MNRAS **000**, 1–14 (2020) Preprint 15 August 2022 Compiled using MNRAS LATEX style file v3.0

# Benchmarking the spectroscopic masses of 253 evolved stars using asteroseismology with TESS

Sai Prathyusha Malla[1]★, Dennis Stello[1,2,3], Benjamin T. Montet[1], Daniel Huber[4], Marc Hon[1,4], Timothy R. Bedding[2,3], Claudia Reyes[1], Daniel R. Hey[2,3]
[1]School of Physics, The University of New South Wales, Sydney NSW 2052, Australia
[2]Sydney Institute of Astronomy(SIfA), School of Physics, University of Sydney, NSW 2006, Australia
[3]Stellar Astrophysics Centre, Dept. of Physics and Astronomy, Aarhus University, Ny Munkegade, DK- 8000 Aarhus C, Denmark.
[4]Institute for Astronomy, University of Hawai'i, 2680 Woodlawn Drive, Honolulu, HI 96822, USA

Accepted XXX. Received YYY; in original form ZZZ

**ABSTRACT**

One way to understand planet formation is through studying the correlations between planet occurrence rates and stellar mass. However, measuring stellar mass in the red giant regime is very difficult. In particular, the spectroscopic masses of certain evolved stars, often referred to as "retired A-stars", have been questioned in the literature. Efforts to resolve this mass controversy using spectroscopy, interferometry and asteroseismology have so far been inconclusive. A recent ensemble study found a mass-dependent mass offset, but the result was based on only 16 stars. With NASA's Transiting Exoplanet Survey Satellite (TESS), we expand the investigation of the mass discrepancy to a total of 93 low-luminosity stars, synonymous with the retired A-stars. We measure their characteristic oscillation frequency, $\nu_{\rm max}$, and the large frequency separation, $\Delta\nu$, from their TESS photometric time series. Using these measurements and asteroseismic scaling relations, we derive asteroseismic masses and compare them with spectroscopic masses from five surveys, to comprehensively study the alleged mass-dependent mass offset. We find a mass offset between spectroscopy and seismology that increases with stellar mass. However, we note that adopting the seismic mass scale does not have a significant effect on the planet occurrence-mass-metallicity correlation for the so-called retired A-stars. We also report seismic measurements and masses for 160 higher luminosity giants (mostly helium-core-burning) from the spectroscopic surveys and provide a catalog of asteroseismic masses for 253 unique stars.

**Key words:** keyword1 – keyword2 – keyword3

## 1 INTRODUCTION

Correlations between the planet occurrence rates and host star properties, in particular stellar mass, can inform us about planet formation (e.g., see Fischer & Valenti 2005, Johnson et al. 2010, Dawson & Johnson 2018, Ghezzi et al. 2018). For this, it is important to sample stars across a large range of masses, including those significantly more massive than the Sun. However, the main sequence A- and hot F-type stars have broad spectral lines making radial velocity measurements less precise. Hence, radial velocity planet searches have been biased against intermediate-mass A- and hot F-type stars. To circumvent this difficulty in finding planets around the intermediate-mass A- and hot F-type stars, Johnson et al. (2006) set out to find planets around their cooler, more evolved counterparts in the subgiant and red giant regimes. They referred to these stars as "retired A"-stars. However, A- and F-progenitors that ascend the red giant branch become difficult to distinguish in temperature ($T_{\rm eff}$) and luminosity (L) from their G- and K- counterparts, leaving stellar mass as the only way to differentiate between these stars. Thus, accurately determining the stellar mass of these evolved stars is important.

Traditionally, stellar masses are determined using spectroscopy and grid-based modelling. Lloyd (2011) compared the masses of a selection of evolved planet-hosting stars from the Exoplanet Orbit Database[1] (Wright et al. 2011) with a sample of field stars with similar mass ($M$) and surface gravity ($\log g$) from the catalogs by Allende Prieto & Lambert (1999) and Glebocki & Gnacinski (2005). Lloyd (2011) discovered a discrepancy between the mass distributions for the samples of evolved planet-hosting stars from the Exoplanet Orbit Database and the field stars and suggested the

★ E-mail: s.malla@student.unsw.edu.au (UNSW)

[1] www.exoplanets.org

masses of these evolved planet-hosting stars were overestimated by up to 50%. They attributed the deficit of massive evolved planet-hosting stars in their sample to the differences in evolution speeds of stars with different stellar masses. Massive stars evolve faster than less massive stars and are hence less common, and the failure to account for this difference in evolution speeds of stars in grid-based modelling may lead to erroneous determination of the stellar mass.

Later, Johnson et al. (2013) benchmarked their apparent-magnitude-limited subgiant sample against Galactic stellar population models by Girardi et al. (2005) and found no such overestimation in spectroscopic masses. Johnson et al. (2013) argued that their imposed apparent magnitude limit partially counteracted the lower number of massive stars expected from their differential evolution by increasing the relative number of massive stars. However, Lloyd (2013) used apparent magnitude-limited weights for the isochrone integration in his 2011 calculations and argued that irrespective of such limit used in target selection, there was a deficit of massive stars in the subgiant and red giant regime compared to what was reported in the literature. Supporting this argument by Lloyd (2013), Schlaufman & Winn (2013) found consistency between the velocity dispersions for their subgiant sample and their main-sequence F5-G5 sample, but not with their main-sequence A0-F5 sample. This consistency led them to conclude that their subgiants are less massive than main sequence A0-F5 stars.

In addition to the spectroscopy-based mass determinations, the retired A-star mass controversy has been explored using other methods like asteroseismology and interferometry. Asteroseismology, in particular, can provide us with precise model-independent stellar masses (Stello et al. 2008; Kallinger et al. 2010; Chaplin & Miglio 2013; Gaulme et al. 2016; Huber et al. 2017; Yu et al. 2018) while long-baseline interferometry provides better constraints on effective temperatures and radii, thus reducing systematic errors in model-dependent stellar mass determinations (White et al. 2018). Johnson et al. (2014) made the first attempt to use asteroseismology to test the spectroscopic mass of HD 185351–the only known intermediate-mass evolved planet-hosting star observed by *Kepler* (Borucki et al. 2010). However, they could not reconcile their stellar mass measurements from spectroscopy, asteroseismology and interferometry. The reconciliation was later achieved by Hjørringgaard et al. (2017) with a more comprehensive asteroseismic modelling. They found an overestimation of about $\sim 15\%$ in the spectroscopic mass of HD 185351. Similarly, for seven of the eight evolved planet-hosting stars observed using the ground-based Stellar Observations Network Group (SONG, Andersen et al. 2016) telescope, Stello et al. (2017) found an overestimation of 15–20% in spectroscopic masses compared to the corresponding seismic masses. Additionally, using interferometry for five evolved planet-hosting stars, White et al. (2018) found the spectroscopic masses from the literature to be 15% larger than their interferometry-based values. On the other hand, contrary to the above evidence suggesting the presence of a mass offset, Campante et al. (2017, 1 star) and North et al. (2017, 7 stars) found no apparent difference between the spectroscopic and seismic masses in their samples of stars, of which not all were hosting planets. Ghezzi & Johnson (2015) investigated the presence of a mass offset with 59 evolved stars using model-independent masses from binary systems (26 stars) and asteroseismology (33 stars) and found no significant evidence for it. Later, Ghezzi et al. (2018, 245 stars) arrived at the same conclusion from their spectroscopic and kinematic analyses.

Malla et al. (2020) performed an ensemble study to understand why some seismic studies found a discrepancy between the spectroscopic and seismic mass scales while others did not. They combined their seismic results for four evolved planet-hosting stars with 12 other stars studied by Stello et al. (2017) and North et al. (2017). From three different spectroscopic sources (Mortier et al. 2013; Jofré et al. 2015; Stock et al. 2018), they found that stars above a mass threshold of 1.6 $M_\odot$ had a significant mass offset, while those below the threshold did not. This result is consistent with the findings by Stello et al. (2017) and North et al. (2017). The transition mass of $\sim 1.6\,M_\odot$ is the same as the one that separates fast and slow-moving evolving stars in the subgiant regime where most of the retired A-stars lie. However, the Malla et al. (2020) ensemble study only had relatively few stars with masses below 1.0 $M_\odot$ and above 1.6 $M_\odot$, leading to an inconclusive result. More stars across a wider mass range would be required to make firmer conclusions about such mass-dependent offset. Fortunately, with the launch of the Transiting Exoplanet Survey Satellite (TESS, Ricker et al. 2016), we now have high-cadence time-resolved data for many more stars with spectroscopically-derived masses. Hence, we can use TESS to measure the asteroseismic-based masses of these stars.

In this paper, we expand the sample of evolved stars for which we can test the previous spectroscopic mass determinations against seismically determined masses, and to provide more stars in the mass range poorly covered by Malla et al. (2020). For this purpose, we use the photometric data from the first three years of the TESS mission and asteroseismic scaling relations to determine the seismic masses of these stars. With this large data set, we further expand the scope of the mass offset found by Malla et al. (2020) towards up to five different spectroscopic sources. In Section 2, we discuss the selection criteria for our targets. We measure our global seismic parameters in Section 3 and our seismic masses in Section 4. In Section 5, we discuss the mass discrepancy between spectroscopic and seismic mass scales guided by our results. In Section 6, we draw conclusions based on our findings.

## 2 TARGET SELECTION AND OBSERVATIONS

We selected 451 evolved stars that had spectroscopic masses previously studied by either Mortier et al. (2013, M13), Jofré et al. (2015, J15), Wittenmyer et al. (2016, W16), Ghezzi et al. (2018, G18), or by Stock et al. (2018, S18) and that were observed in 2-minute cadence during the first three years of the TESS mission. Table 1 (Column 2) shows the total number of unique stars in our sample, along with the number of stars analyzed from each spectroscopic survey. Fig. 1 shows the colour-magnitude diagram for the 451 stars in our sample along with solar-metallicity BaSTI tracks [2] (Pietrinferni et al. 2004) to guide the eye. Of the five chosen spectroscopic sources, M13, J15, and S18 studied evolved stars and were previously used to study the mass offset by Malla et al. (2020). G18 studied evolved stars (both planet-hosting and non-planet-hosting) to derive a planet occurrence-mass-metallicity correlation, while W16 studied the retired A-stars as observed from the southern hemisphere. In Table 2, we list the spectroscopic mass range covered by our sample from each source and in Table 3, we list the spectroscopic masses of the stars for each spectroscopic source. From Fig. 2 and also Table 3 (Columns 6–10), we can see that 22 stars are studied by multiple spectroscopic sources. Such stars are plotted multiple times in Fig. 1.

[2] http://basti.oa-teramo.inaf.it/

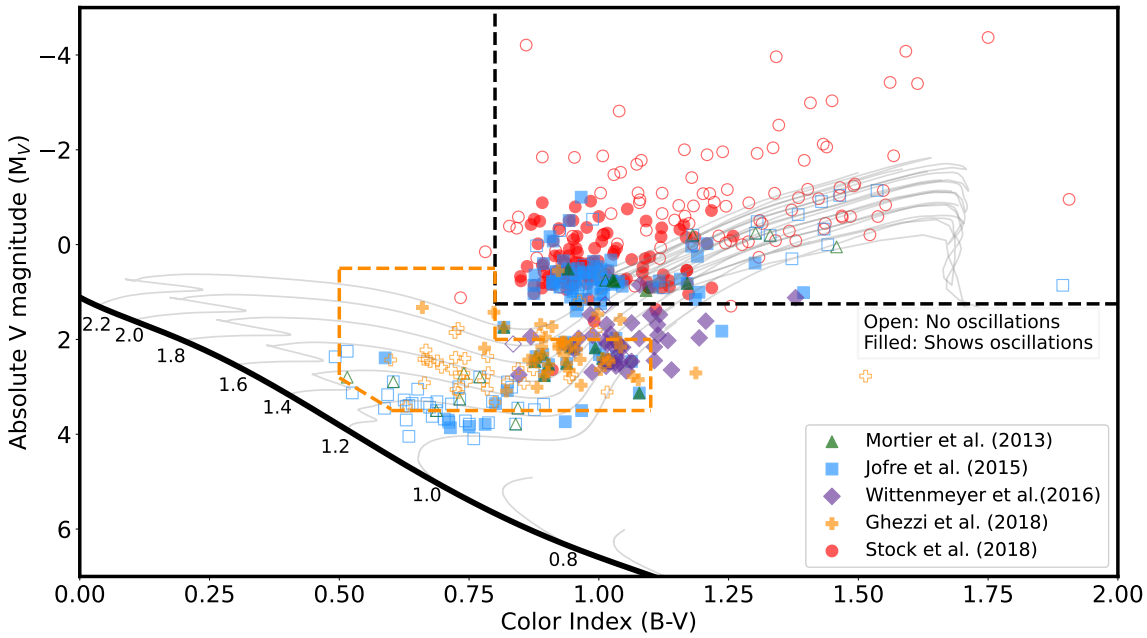


**Figure 1.** Color-magnitude diagram of the 451 stars in our sample plotted along the solar-metallicity BaSTI evolutionary tracks (Pietrinferni et al. 2004). Each point represents a star and is colour-coded according to the spectroscopic source to which it belongs. Green triangles represent the stars previously studied by M13, blue squares by J15, purple diamonds by W16, orange pluses by G18 and red circles by S18. Stars that were studied by multiple spectroscopic sources are plotted multiple times. A list of the overlapping stars can be inferred from Table 3 (Columns 6–10). The solid black line is the averaged Hipparcos main-sequence defined by Wright (2005). The dashed black line corresponds to the boundary between the low- and high- luminosity stars in the CMD according to the criteria listed in Section 5. The area surrounded by dashed orange lines corresponds to the initial selection criteria employed by G18. For stars TIC 356000102, TIC 258873063, TIC 471011913 and TIC 471012056, B magnitude values were not available from the Tess Input Catalog and hence, the $B_T$ and $V_T$ values from the Hipparcos catalog (Høg 2000) were used.

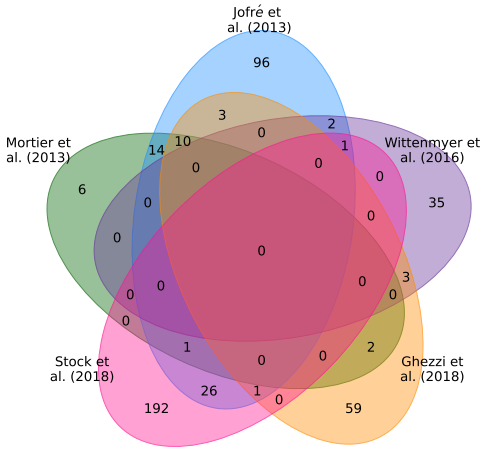


**Figure 2.** Venn diagram representing the 451 stars studied by the five spectroscopic sources: Mortier et al. (2013, M13), Jofré et al. (2015, J15), Wittenmyer et al. (2016, W16), Ghezzi et al. (2018, G18) and Stock et al. (2018, S18).

To distinguish between what can be viewed as subgiants/early red giant branch stars (low-luminosity sample), akin to the retired A-star sample, and the more evolved red giant branch and red clump stars (high-luminosity sample), we define the stars with absolute magnitude $M_V < 1.25$ and colour $B-V > 0.8$ to be high-luminosity stars (represented by the dashed black line in Fig. 1). The remaining stars are considered low-luminosity stars. Of the 451 stars in our sample, we find 283 high-luminosity and 168 low-luminosity stars based on the criteria above. A spectroscopic-source-wise breakdown of the low- and high-luminosity stars is provided in Table 1. We also mark individual stars as a low- or high-luminosity stars in Table 3 (Column 11).

The selected targets had at least ~ 27 days (one sector) of TESS data available.[3] The targets were observed in a 2-minute cadence, and the data was downloaded from the TESS Asteroseismic Science Operations Center (TASOC) website.[4] For our analysis, we used the corrected light curves (PDCMAP) provided by the TESS Science Processing Operations Center (SPOC) (Jenkins et al. 2016), which uses a pipeline similar to the Kepler Science Operations Center (KSOC) pipeline. Table 3 (Columns 4 and 5) lists the TESS magnitudes and the observing coverage of our targets.

[3] The stars close to the ecliptic plane ($|\beta| \lesssim 6$ deg) are not in our sample as TESS did not observe this section during the prime mission.
[4] https://tasoc.dk/

**Table 1.** Star counts for TESS-spectroscopic overlap sample

| Spectroscopic source | $N_{obs}$ | $N_{osc}$ | $N_{obs,low}$ | $N_{osc,low}$ | $N_{obs,high}$ | $N_{osc,high}$ |
|---|---|---|---|---|---|---|
| (1) | (2) | (3) | (4) | (5) | (6) | (7) |
| **Total unique stars** | 451 | 253 | 168 | 93 | 283 | 160 |
| M13 | 33 | 19 | 22 | 14 | 11 | 5 |
| J15 | 154 | 93 | 66 | 31 | 88 | 62 |
| W16 | 41 | 38 | 39 | 36 | 2 | 2 |
| G18 | 78 | 42 | 76 | 41 | 2 | 1 |
| S18 | 222 | 119 | 8 | 5 | 214 | 114 |

Notes:
$N_{obs}$: Number of stars observed by TESS
$N_{osc}$: Number of oscillating stars
$N_{obs,low}$: Number of low-luminosity stars observed by TESS
$N_{osc,low}$: Number of oscillating low-luminosity stars
$N_{obs,high}$: Number of high-luminosity stars observed by TESS
$N_{osc,high}$: Number of oscillating high-luminosity stars
M13 : Mortier et al. (2013)
J15 : Jofré et al. (2015)
W16 : Wittenmyer et al. (2016)
G18 : Ghezzi et al. (2018)
S18 : Stock et al. (2018)
A machine-readable version of the table is available online on CDS.

We first excluded any known anomalies (e.g., due to cosmic rays or stray light) by only using data with a zero pixel-quality flag as marked by the SPOC pipeline. The resulting light curves were subjected to a highpass filter of ~3 $\mu$Hz (~4 days) to remove any slow trends. For stars 24 Sex and HD 185351, the quality of the time series was poor and showed trends with periods less than ~4 days, which interfered with the detection of oscillations. Hence, we used a ~50 $\mu$Hz highpass filter for these two stars. We then performed a 4-$\sigma$ clipping to remove significant outliers from the light curves. For seven stars, we also removed any strong features (e.g., dips, flares) to prevent interference with the oscillation detection before applying a highpass filter. To do so, we removed any sudden changes in the mean with amplitudes larger than 4-$\sigma$ of the lightcurve and periods in range of ~0.1–2.5 days. Lastly, we combined the light curves from different sectors by normalizing the flux by dividing out the median on a per-sector basis with the timestamps preserved.

Figs. 3a1 and a2 show the final light curves for 57 Vir and 36 Dor, representative of short and long time series, which were observed by TESS for 1 and 19 sectors, respectively. We use these stars as examples in the following sections.

## 3 EXTRACTION OF GLOBAL SEISMIC PARAMETERS

Similar to Malla et al. (2020), we computed the power density spectra of each light curve using a discrete Fourier transform. Figs. 3b1 and b2 show the power density spectra for 57 Vir and 36 Dor. To measure the frequency of maximum acoustic power $\nu_{max}$ and the large frequency of separation $\Delta\nu$, we used the SYD pipeline[5] (Huber et al. 2009). The SYD pipeline corrects for the granulation background, locates $\nu_{max}$ and measures $\Delta\nu$ from the autocorrelation of the power spectrum. Figs. 3c1 and c2 show the residual power spectra after the granulation background is divided out. The $\nu_{max}$ and $\Delta\nu$ values are tabulated in Table 4 (Columns 4 and 5).

[5] Although the TESS data (sector 8) of 24 Sex has been previously used by Malla et al. (2020), we include this star in our ensemble to include all the available data during the first three years of the prime mission and perform a homogeneous analysis using the SYD pipeline.

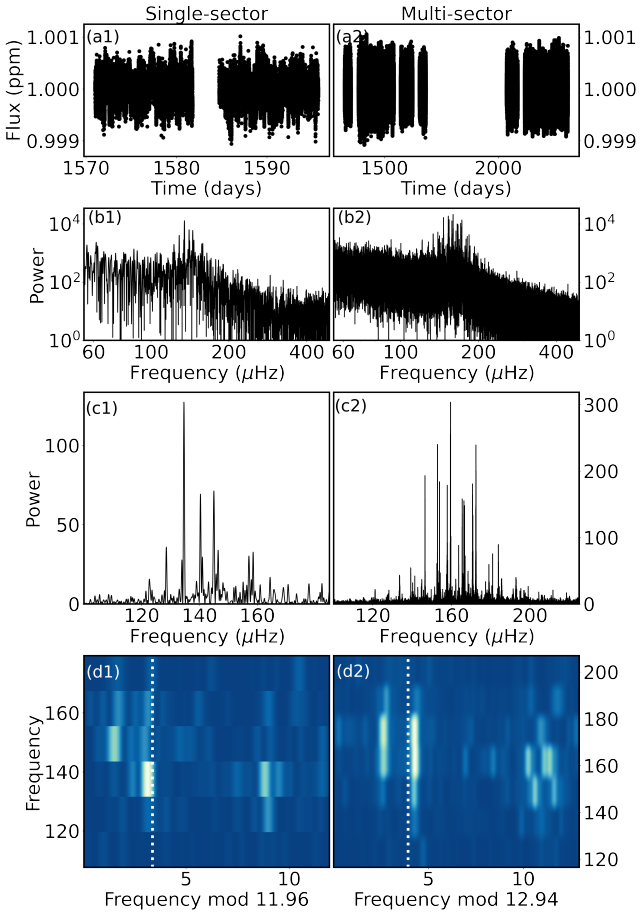


**Figure 3.** Comparison of the SYD results for single-sector (Column 1) and multi-sector (Column 2) data. In Column 1, we present the SYD results for the single-sector 57 Vir data, while Column 2 represents the SYD results for multi-sector 36 Dor data (19 sectors). Row a (Panels a1 and a2) depicts the light curve after combining the multi-sector data (where applicable), removing any known anomalies, and applying a highpass filter with a cut-off frequency of ~3 $\mu$Hz (~4 days) and a 4-$\sigma$ clipping. Row b (Panels b1 and b2) shows the power density spectrum of the corresponding star, and Row c (Panels c1 and c2) depicts the background-corrected power spectrum. Row d (Panels d1 and d2) shows the échelle diagram computed from the smoothed power density spectrum, plotted using the *echelle* module (Hey 2019).

Of the 451 stars analyzed with SYD, we found 253 stars that exhibit solar-like oscillations - 93 low- and 160 high-luminosity stars. Table 1 (Columns 3, 5 and 7, i.e., $N_{osc}$, $N_{low,osc}$, and $N_{high,osc}$) provides a spectroscopic-source-wise breakdown of the solar-like oscillators in our sample.

To verify, and possibly correct, the $\Delta\nu$ measurements by SYD, we used échelle diagrams. The échelle diagrams are obtained by dividing the power density spectrum into segments of length equal

**Table 2.** Spectroscopic mass range covered for TESS-spectroscopic overlap sample

| Spectroscopic source (1) | $M_{spec}$ (2) | $M_{spec,osc}$ (3) | $M^{low}_{spec}$ (4) | $M^{low}_{spec,osc}$ (5) | $M^{high}_{spec}$ (6) | $M^{high}_{spec,osc}$ (7) |
|---|---|---|---|---|---|---|
| M13 | 0.98–2.31 | 1.04–2.31 | 1.08–2.03 | 1.24–2.03 | 0.98–2.31 | 1.04–2.31 |
| J15 | 0.91–3.33 | 0.91–3.23 | 0.91–1.99 | 0.91–1.99 | 0.91–3.33 | 1.01–3.23 |
| W16 | 1.03–2.19 | 1.03–2.19 | 1.03–2.19 | 1.03–2.19 | 1.62–1.66 | 1.62–1.66 |
| G18 | 0.92–2.08 | 0.92–2.08 | 0.92–2.08 | 0.92–2.08 | 1.33–1.86 | 1.33–1.33 |
| S18 | 0.84–6.65 | 0.84–3.23 | 0.96–2.29 | 0.96–1.69 | 0.84–6.65 | 0.84–3.23 |

Notes:
A machine-readable version of the table is available online on CDS.
M13 : Mortier et al. (2013)
J15 : Jofré et al. (2015)
W16 : Wittenmyer et al. (2016)
G18 : Ghezzi et al. (2018)
S18 : Stock et al. (2018)
$M_{spec}$: Spectroscopic mass range for all stars
$M_{spec,osc}$ : Spectroscopic mass for all oscillating stars
$M^{low}_{spec}$ : Spectroscopic mass range for all low luminosity stars
$M^{low}_{spec,osc}$ : Spectroscopic mass range for all oscillating low luminosity stars
$M^{high}_{spec}$ : Spectroscopic mass range for all high luminosity stars
$M^{high}_{spec,osc}$ : Spectroscopic mass range for all oscillating high luminosity stars

**Table 3.** TESS coverage and spectroscopic masses of the targets

| TIC ID | HD | Common name | TESS Magnitude | Number of sectors available | $M_{M13}$ | $M_{J15}$ | $M_{W16}$ | $M_{G18}$ | $M_{S18}$ | Category |
|---|---|---|---|---|---|---|---|---|---|---|
| | | | | | $M_\odot$ | $M_\odot$ | $M_\odot$ | $M_\odot$ | $M_\odot$ | |
| (1) | (2) | (3) | (4) | (5) | (6)[a] | (7)[b] | (8)[c] | (9)[d] | (10)[e] | (11)[f] |
| 612908 | 30856 | - | 7.08 | 2 | 1.36 ± 0.07 | 1.31 ± 0.11 | - | 1.37 ± 0.07 | - | L |
| 1713457 | 90043 | 24 Sex | 5.64 | 2 | 1.81 ± 0.08 | 1.78 ± 0.08 | - | 1.71 ± 0.04 | - | L |
| 5630694 | 103616 | - | 6.90 | 1 | - | - | - | 1.58 ± 0.07 | - | L |
| 11557059 | 7931 | - | 7.01 | 1 | - | - | 1.12 ± 0.25 | 1.3 ± 0.08 | - | L |
| 29921672 | 10011 | - | 7.20 | 1 | - | - | - | 1.54 ± 0.09 | - | L |
| 32550970 | 8407 | - | 6.92 | 1 | - | - | - | 1.13 ± 0.06 | - | L |
| 47336943 | 215049 | - | 7.50 | 1 | - | - | - | 1.42 ± 0.09 | - | L |
| 48401372 | 47562 | - | 7.45 | 2 | - | - | - | 1.63 ± 0.23 | - | L |
| 53873088 | 5608 | - | 5.14 | 1 | 1.66 ± 0.08 | 1.72 ± 0.07 | - | - | - | L |
| 141326842 | 18885 | - | - | 1.91 ± 0.1 | - | - | - | H | | |
| 374828367 | 22796 | 12 Tau | 4.74 | 2 | - | - | - | - | 2.29 ± 0.64 | H |
| 374860864 | 40409 | 36 Dor | 3.75 | 19 | - | - | 1.12 ± 0.25 | - | - | L |
| 422432907 | 115202 | 57 Vir | - | 1.41 ± 0.08 | 1.26 ± 0.25 | - | - | | | |
| 436243682 | 37160 | 40 Ori | 3.21 | 1 | - | 1.07 ± 0.04 | - | - | - | H |

Notes: A machine-readable version of the table for all the 451 stars is available as online downloadable material and from CDS.
[a] Source: Mortier et al. (2013)
[b] Source: Jofré et al. (2015)
[c] Source: Wittenmyer et al. (2016)
[d] Source: Ghezzi et al. (2018)
[e] Source: Stock et al. (2018)
[f] Stars are categorised as low- (L) and high- (H) luminosity stars based on the criteria outlined in Sec. 2

to a trial $\Delta\nu$ and then stacking these segments vertically. The acoustic modes of the same degree form vertical ridges when the trial $\Delta\nu$ corresponds to the correct large frequency separation. We use the SYD $\Delta\nu$ as an initial guess. Figs. 3d1 and d2 depict the échelle diagrams for 57 Vir and 36 Dor respectively. However, the SYD $\Delta\nu$ did not provide good vertical alignment for nine stars (marked in Table 4, Column 5). For these stars, we use the *echelle*[6] module (Hey 2019) to adjust the trial $\Delta\nu$ to the final adopted value guided by the $\Delta\nu$–$\epsilon$ relation by Corsaro et al. (2012). In such a case, we take as our uncertainty the minimum shift in $\Delta\nu$ needed to move the vertical ridges clearly out of alignment (an illustration of this can be seen in Fig. 5 of Stello et al. 2011). We find an average uncertainty of 0.165 $\mu$Hz for these nine stars. Table 4 (Column 5) lists the final $\Delta\nu$ observed for our targets. Despite our attempts to achieve a good vertical mode alignment using SYD pipeline and/or *echelle* module, we could only make a tentative detection of $\Delta\nu$ for 19 stars. Such stars are also marked in Table 4 (Column 5).

[6] https://pypi.org/project/echelle/

**Table 4.** Observed parameters **and TIC-based seismic mass results** for our targets

| TIC ID | HD | $T_{\rm eff}$ [K] | $\nu_{\rm max,obs,SYD}$ [$\mu$Hz] | $\Delta\nu_{\rm obs,SYD}$ [$\mu$Hz] | $M_{\rm seis,phot}$ [$M_\odot$] | $R_{\rm seis,phot}$ [$R_\odot$] | Source of Parallax |
|---|---|---|---|---|---|---|---|
| (1) | (2) | (3)[a] | (4) | (5) | (6) | (7) | (8) |
| 612908 | 30856 | 4895.00 | 167.59 ± 1.96 | 13.64 ± 0.05 | 1.19 ± 0.1 | 4.9 ± 0.07 | Gaia eDR3 |
| 1713457 | 90043 | 5027.00 | 191.34 ± 4.94 | 13.88 ± 0.11 | 1.47 ± 0.12 | 5.47 ± 0.17 | Gaia eDR3 |
| 5630694 | 103616 | 5009.00 | 416.04 ± 6.63 | 30.54 ± 0.16 | 1.25 ± 0.11 | 2.45 ± 0.05 | Gaia eDR3 |
| 11557059 | 7931 | 4796.00 | 160.49 ± 3.46 | 13.17 ± 0.09 | 1.11 ± 0.09 | 4.98 ± 0.13 | Gaia eDR3 |
| 29921672 | 10011 | 5025.00 | 212.34 ± 5.21 | 15.19 ± 0.2 | 1.2 ± 0.11 | 5.07 ± 0.18 | Gaia eDR3 |
| 32550970 | 8407 | 4922.00 | 101.15 ± 1.93 | 5.25 ± 0.19 | 1.25 ± 0.1 | 20.0 ± 1.48 | Gaia eDR3 |
| 47336943 | 215049 | 5108.00 | 470.78 ± 12.48 | 29.3 ± 0.09 | 1.29 ± 0.11 | 3.05 ± 0.08 | Gaia eDR3 |
| 48401372 | 47562 | 4976.00 | 133.48 ± 4.41 | 11.13 ± 0.11 | 1.27 ± 0.11 | 5.91 ± 0.23 | Gaia eDR3 |
| 53873088 | 5608 | 4877.00 | 157.49 ± 15.56 | 12.77 ± 0.48 | 1.17 ± 0.49 | 5.24 ± 0.65 | Gaia DR2 |
| 141326842 | 18885 | 4724.63 | 46.62 ± 0.87 | 4.4 ± 0.2[b] | 1.78 ± 0.41 | 12.86 ± 1.19 | Gaia DR2 |
| 374828367 | 22796 | 5014.00 | 58.36 ± 2.34 | 5.43 ± 0.12 | 1.95 ± 0.51 | 10.88 ± 0.66 | Gaia DR2 |
| 374860864 | 40409 | 4806.00 | 161.84 ± 1.08 | 12.94 ± 0.05[b] | 1.03 ± 0.28 | 5.21 ± 0.05 | *Hipparcos* |
| 422432907 | 115202 | 4889.00 | 139.5 ± 1.81 | 11.96 ± 0.11[b] | 1.15 ± 0.3 | 5.3 ± 0.12 | *Hipparcos* |
| 436243682 | 37160 | 4825.83 | 41.73 ± 1.01 | 4.2 ± 0.55[c] | 0.78 ± 0.19 | 12.77 ± 3.34 | *Hipparcos* |

Note: A machine-readable version of the table for all the 253 oscillating stars is available as online downloadable material and from CDS.
[a] Source: TESS Input Catalogue (Stassun et al. 2018). We adopted an uncertainty of 100 K in the effective temperature (Thygesen et al. 2012).
[b] $\Delta\nu$ found using the *echelle* module.
[c] Tentative detection of $\Delta\nu$.

**Table 5.** Seismic masses for our targets derived using spectroscopic parameters

| TIC ID | HD | L [$L_\odot$] | $M_1$ [$M_\odot$] | $M_2$ [$M_\odot$] | $M_3$ [$M_\odot$] | Spectroscopic source used |
|---|---|---|---|---|---|---|
| (1) | (2) | (3) | (4) | (5) | (6) | (7) |
| 612908 | 30856 | 12.61 ± 0.07 | 1.16 ± 0.08 | 1.15 ± 0.01 | 1.18 ± 0.04 | G18 |
| | 30856 | 12.85 ± 0.07 | 1.16 ± 0.08 | 1.14 ± 0.01 | 1.2 ± 0.05 | M13 |
| | 30856 | 12.46 ± 0.07 | 1.17 ± 0.08 | 1.17 ± 0.01 | 1.17 ± 0.04 | J15 |
| 1713457 | 90043 | 13.69 ± 0.07 | 1.4 ± 0.1 | 1.28 ± 0.02 | 1.67 ± 0.14 | G18 |
| | 90043 | 14.2 ± 0.07 | 1.39 ± 0.1 | 1.24 ± 0.02 | 1.73 ± 0.14 | M13 |
| | 90043 | 13.94 ± 0.07 | 1.39 ± 0.1 | 1.26 ± 0.02 | 1.7 ± 0.14 | J15 |
| 5630694 | 103616 | 10.61 ± 0.07 | 2.11 ± 0.15 | 3.42 ± 0.05 | 0.81 ± 0.04 | G18 |
| 11557059 | 7931 | 11.2 ± 0.07 | 1.1 ± 0.08 | 1.09 ± 0.02 | 1.12 ± 0.08 | G18 |
| | 7931 | 11.22 ± 0.07 | 1.1 ± 0.08 | 1.09 ± 0.02 | 1.12 ± 0.08 | W18 |
| 29921672 | 10011 | 13.81 ± 0.07 | 1.45 ± 0.11 | 1.35 ± 0.04 | 1.69 ± 0.15 | G18 |
| 32550970 | 8407 | 23.04 ± 0.09 | 1.27 ± 0.09 | 1.18 ± 0.01 | 1.47 ± 0.08 | G18 |
| 47336943 | 215049 | 5.66 ± 0.05 | 1.27 ± 0.09 | 1.21 ± 0.02 | 1.4 ± 0.11 | G18 |
| 48401372 | 47562 | 18.06 ± 0.09 | 1.26 ± 0.1 | 1.2 ± 0.03 | 1.36 ± 0.15 | G18 |
| 53873088 | 5608 | 13.3 ± 0.42 | 1.24 ± 0.11 | 1.1 ± 0.05 | 1.59 ± 0.24 | M13 |
| | 5608 | 12.99 ± 0.42 | 1.25 ± 0.12 | 1.12 ± 0.05 | 1.56 ± 0.23 | J15 |
| 141326842 | 18885 | 60.68 ± 0.39 | 1.74 ± 0.13 | 0.46 ± 1.08 | 24.31 ± 112.68 | J15 |
| 374828367 | 22796 | 63.23 ± 0.45 | 1.93 ± 0.16 | 1.87 ± 0.09 | 2.06 ± 0.31 | S18 |
| 374860864 | 40409 | 10.98 ± 0.27 | 1.06 ± 0.08 | 1.05 ± 0.04 | 1.07 ± 0.0 | W18 |
| 422432907 | 115202 | 12.97 ± 0.28 | 1.05 ± 0.08 | 1.01 ± 0.23 | 1.13 ± 0.51 | J15 |
| | 115202 | 12.11 ± 0.27 | 1.07 ± 0.08 | 1.09 ± 0.25 | 1.05 ± 0.47 | W18 |
| 436243682 | 37160 | 28.24 ± 0.35 | 0.7 ± 0.05 | 0.44 ± 0.11 | 1.81 ± 0.95 | J15 |

Note: A machine-readable version of the table for all the 253 stars is available as online downloadable material and from CDS.
$M_1$ : $\nu_{\rm max}$-only based seismic mass derived using Eq. 1
$M_2$ : $\Delta\nu$-only based seismic mass derived using Eq. 2
$M_3$ : $\nu_{\rm max}$ and $\Delta\nu$- based seismic mass derived using Eq. 3
M13 : Mortier et al. (2013)
J15 : Jofré et al. (2015)
W16 : Wittenmyer et al. (2016)
G18 : Ghezzi et al. (2018)
S18 : Stock et al. (2018)

## 4 DETERMINING STELLAR MASS

We use two asteroseismic scaling relations to determine three seismic masses: one based on $\nu_{\rm max}$, one based on $\Delta\nu$, and one based on $\nu_{\rm max}$ and $\Delta\nu$. The $\nu_{\rm max}$-only based mass uses the relation between $\nu_{\rm max}$ and the acoustic cutoff frequency (Brown et al. 1991; Kjeldsen & Bedding 1995). Following Stello et al. (2008), this leads to the following relation for mass:

$$\frac{M}{\rm M_\odot} \simeq \left(\frac{\nu_{\rm max}}{\nu_{\rm max,\odot}}\right)^{-1} \left(\frac{T_{\rm eff}}{\rm T_{eff,\odot}}\right)^{-3.5} \left(\frac{L}{\rm L_\odot}\right). \quad (1)$$

To be consistent with Stello et al. (2017) and Malla et al. (2020), we use $\nu_{\rm max,\odot}$ = 3090 $\mu$Hz and $\rm T_{eff,\odot}$ = 5777K (Huber et al. 2009).

We also know that $\Delta\nu$ scales with the square root of stellar mean density (Ulrich 1986). Hence, we compute a $\Delta\nu$-only based seismic mass as follows:

$$\frac{M}{\rm M_\odot} \simeq \left(\frac{\Delta\nu}{\rm f_{\Delta\nu}\Delta\nu_\odot}\right)^{2} \left(\frac{T_{\rm eff}}{\rm T_{eff,\odot}}\right)^{-6} \left(\frac{L}{\rm L_\odot}\right)^{1.5}. \quad (2)$$

Here $f_{\Delta\nu}$ is a necessary correction factor applied to the scaling relation linking $\Delta\nu$ and density. We use the software *asfgrid*[7] by Sharma et al. (2016) to obtain the correction factor.

By combining Eq. 2 with Eq. 1, we measure a seismic mass using both $\nu_{\rm max}$ and $\Delta\nu$ with very little dependence on $T_{\rm eff}$ and eliminating the need for a luminosity determination, which for data with good $\Delta\nu$ measurements, like those from *Kepler*, has been the most common way to determine seismic masses on large ensembles (see Kallinger et al. 2010, Pinsonneault et al. 2014, Serenelli et al. 2017, Pinsonneault et al. 2018 and Yu et al. 2018):

$$\frac{M}{\rm M_\odot} \simeq \left(\frac{\nu_{\rm max}}{\nu_{\rm max,\odot}}\right)^{3} \left(\frac{\Delta\nu}{\rm f_{\Delta\nu}\Delta\nu_\odot}\right)^{-4} \left(\frac{T_{\rm eff}}{\rm T_{eff,\odot}}\right)^{1.5}. \quad (3)$$

### 4.1 Using spectroscopy

To perform a like-for-like comparison between the spectroscopic-based isochrone masses from the literature and our seismic masses, we adopt the spectroscopic parameters ($T_{\rm eff}$ and [Fe/H]) determined from each spectroscopic survey to derive the seismic masses using the seismic scaling relations (Eqs. 1, 2 and 3).

We used *isoclassify*[8] (Huber et al. 2017; Berger et al. 2020) to compute luminosities for the solar-like oscillators in our sample. We used the spectroscopic parameters ($T_{\rm eff}$ and [Fe/H]) from the corresponding spectroscopic source (M13, J15, W16, G18 or S18). We also adopted Gaia eDR3 parallaxes (Gaia Collaboration et al. 2016, 2022a) for stars in the magnitude range 6 < G < 21 (57 stars), Gaia DR2 parallaxes (Gaia Collaboration et al. 2018) for stars with 5 ≤ G ≤ 6 (100 stars) and Hipparcos parallaxes for the rest (van Leeuwen 2007, 96 stars). The source of parallax used for each star is marked in Table 4 (Column 8). We discuss our choice of parallaxes in more detail in Appendix B. We also used the 2MASS Ks magnitude as an input. If the 2MASS Ks magnitudes were unavailable, we used the Tycho $\rm V_T$ photometry. We set the *dustmap* parameter to 'allsky' to use a combination of reddening maps (Drimmel et al. 2003, Marshall et al. 2006, Green et al. 2015 and Bovy et al. 2016) to provide full sky coverage as implemented in the *mwdust* package by Bovy et al. (2016). Table 5 (Column 3) shows the resulting luminosities using the spectroscopic parameters from each spectroscopic source.

[7] https://ascl.net/1603.009
[8] https://github.com/danxhuber/isoclassify

Now, with all the input for the scaling relations at hand, we derived the three seismic masses $M_1$, $M_2$ and $M_3$ from Eqs. 1, 2 and 3 using the spectroscopic parameters from M13, J15, W16, G18 and S18. We list the seismic masses in Table 5 (Columns 4–6) for each spectroscopic source. We will compare these seismic masses to their corresponding spectroscopic masses in Section 5.

### 4.2 Using the TESS Input Catalog

In addition to comparing our seismic masses to spectroscopy, a secondary aim of the paper is to provide a catalog of seismic masses for solar-like oscillators in our sample. However, a single spectroscopic source does not cover all solar-like oscillators. Hence, we used the characteristic frequency $\nu_{\rm max}$ and *isoclassify*-based luminosities in Eq. 1 to construct a homogenous catalog of seismic masses that have very little dependence on models. Similar to Section 4.1, we also use Gaia eDR3 and DR2 parallaxes (and *Hipparcos* parallaxes where Gaia parallaxes are not applicable) as outlined in Appendix B and 2MASS Ks (or Tycho $V_{\rm T}$) magnitudes as input. However, we use the effective temperatures from the TESS Input Catalog (TIC) instead of our previously adopted spectroscopic $T_{\rm eff}$. The TIC refers to $T_{\rm eff}$ from spectroscopic sources (listed in Table 1 by Stassun et al. 2018, 190 solar-like oscillators) and Gaia DR2 photometry (60 solar-like oscillators), preferring the former to the latter if available. Three stars (TIC 60857616, TIC 352542468, TIC 408048857) do not have $T_{\rm eff}$ measurements in TIC. For stars TIC 60857616 and TIC 408048857, we used the $T_{\rm eff}$ value by Stock et al. (2018) and for star TIC 352542468, we used the value from Wittenmyer et al. (2016). Table 4 (Column 6, $M_{\rm seis,phot}$) lists these TIC-based seismic masses for the 253 solar-like oscillators.

In addition to measuring seismic mass, we also obtained radius by rearranging the seismic scaling relations (Kallinger et al. 2010):

$$\frac{R}{\rm R_\odot} \simeq \left(\frac{\nu_{\rm max}}{\nu_{\rm max,\odot}}\right) \left(\frac{\Delta\nu}{\rm f_{\Delta\nu}\Delta\nu_\odot}\right)^{-2} \left(\frac{T_{\rm eff}}{\rm T_{eff,\odot}}\right)^{0.5}. \quad (4)$$

For stars with reliable $\Delta\nu$ measurement, we can determine the star's radius using the above relation. Because there is no single source of metallicities available for our entire sample, we did not correct $\Delta\nu$ using *asfgrid* and set the correction factor $f_{\Delta\nu}$ to 1 in Eq. 4. We list the seismic radii thus obtained in Table 4 (Column 7, $R_{\rm seis,phot}$). To use the radii in spectroscopic analyses, we advise them to be corrected using an appropriate $f_{\Delta\nu}$ in Eq. 4.

To avoid systematics and to quantify the difference between our spectroscopic and TIC-based $T_{\rm eff}$, we plot in Fig. 4 the fractional difference between spectroscopic and TIC-based effective temperature as a function of the spectroscopic $T_{\rm eff}$. From the plot, we find an uncertainty-weighted average of the fractional difference to be 0.02 for M13, 0.008 for J15, 0.002 for W16, 0.009 for G18 and -0.007 for S18, implying that the spectroscopic and TIC-based $T_{\rm eff}$ agree with each other within 2 %, and typically within 1%.

## 5 MASS COMPARISON

### 5.1 Mass-dependent mass offset in low-luminosity stars

Of the 168 low-luminosity stars, 93 show solar-like oscillations (Table 1, columns 4 and 5). With this large ensemble of stars, we now investigate the mass discrepancy between the spectroscopic and seismic masses by plotting the difference between the two mass scales as a function of the spectroscopic mass, as depicted in Fig. 5.

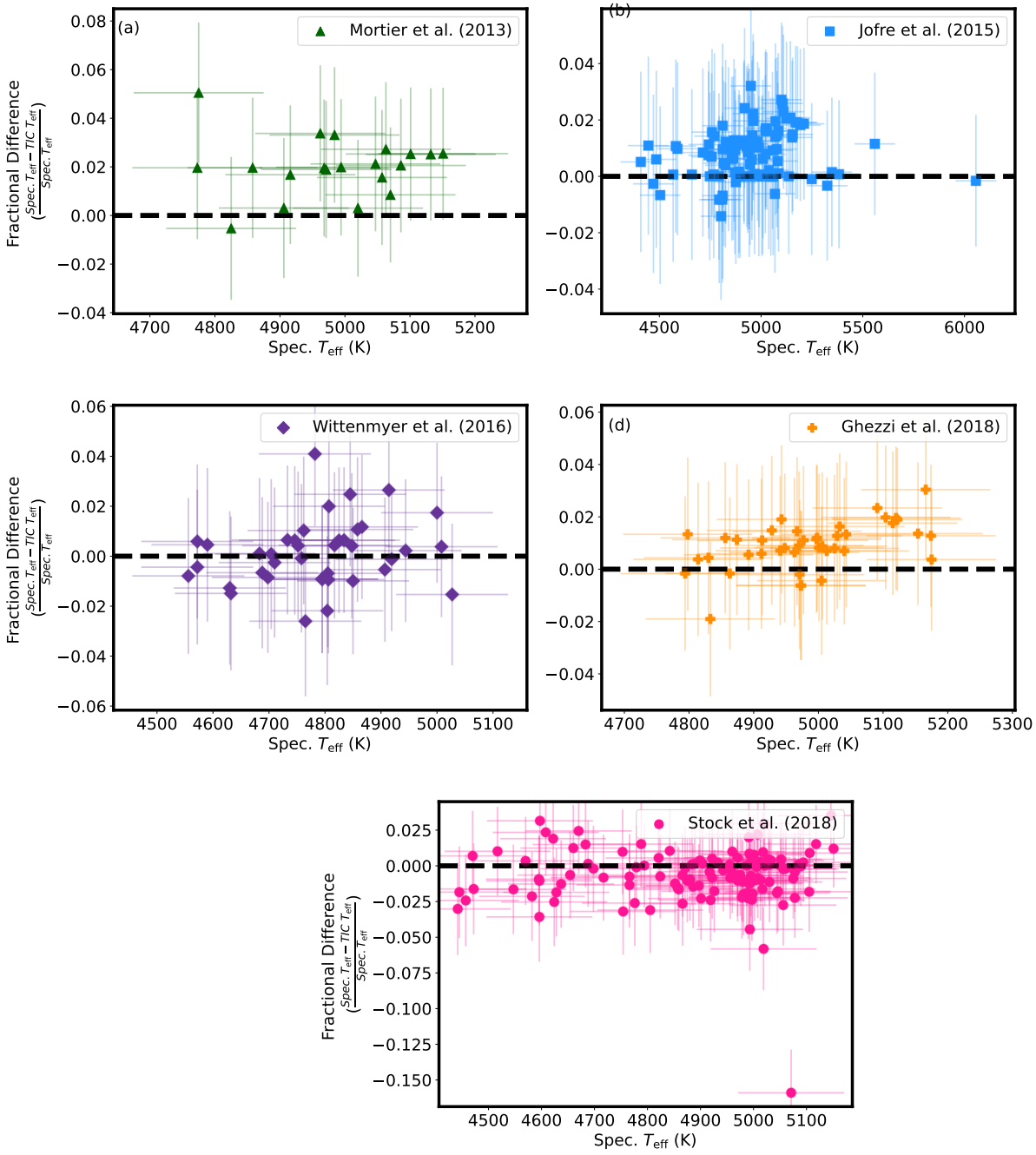


**Figure 4.** Difference between the spectroscopic and TIC $T_{\rm eff}$ plotted as a function of spectroscopic $T_{\rm eff}$ for 253 solar-like oscillators in our sample for (a) M13 (b) J15 (c) W16 (d) G18 (e) S18. The dashed black line represents no difference between the spectroscopic and TIC $T_{\rm eff}$.

Here, we plot all the five different spectroscopic sources together.[9] In Fig. 5a1, we use the $\nu_{max}$-only based seismic masses ($M_1$) while Figs. 5b1, and c1 use the $\Delta\nu$-based and $\nu_{max}$- and $\Delta\nu$-based seismic masses ($M_2$ and $M_3$) respectively. The 22 low-luminosity stars listed in Table 3 appear in more than one of our spectroscopic sources and are plotted multiple times.

Fig. 5 shows a mass-dependent mass offset, with larger offsets for more massive stars, in agreement with the results by Malla et al. (2020). By comparing Figs. 5a1, b1, and c1, we see a smaller scatter (hence, a tighter relation) in the mass offset when using Eq. 1 to derive seismic mass (Fig. 5, Row a), which suggests that this relation provides more robust results in an ensemble sense. This result agrees with the conclusion by Miglio et al. (2016), who looked at the same three different seismic mass scales we use here but on nearly equal-mass cluster red giants. Another thing we notice by comparing Figs. 5a1, b1, and c1 is that the uncertainty-weighted average of the mass offset is not the same for all three seismic masses. The averaged mass offset is 0.15 $M_\odot$ for $M_1$, 0.24 $M_\odot$ for $M_2$, and 0.08 $M_\odot$ for $M_3$. We know that the three asteroseismic mass scaling relations have different sensitivities in $T_{eff}$. We, therefore, tried to see if we could get a better agreement between the three seismic mass scales by shifting the $T_{eff}$ scale. We found that decreasing $T_{eff}$ by 150 K made the agreement much better with average mass offsets now being 0.12 $M_\odot$ for $M_1$, 0.15 $M_\odot$ for $M_2$, and 0.18 $M_\odot$ for $M_3$ (Fig. 5, column 2). This result includes the change we get in inferred luminosity from *isoclassify* when adopting this cooler $T_{eff}$ scale. We note that this $T_{eff}$ shift is comparable to our adopted $T_{eff}$ uncertainty (100 K, Thygesen et al. 2012). Despite employing the $T_{eff}$-offset, we notice that the mass-dependent mass offset persists, as we can see from our Figs. 5a2, b2 and c2. Because the scaling relations also depend on luminosities, we tried to reconcile the average mass offsets for the three seismic masses ($M_1$, $M_2$, and $M_3$) by changing luminosity under the assumption that there is no parallax offset or $T_{eff}$-offset. However, this required increasing luminosity by 0.5 $L_\odot$, which is beyond what we expect from the systematic parallax errors (Lindegren et al. 2018; Zinn et al. 2019b; Gaia Collaboration et al. 2018).

To quantify the mass-dependent mass offset, we fitted polynomials of varying orders and a step function (following a suggestion by Malla et al. 2020) to the mass offset without $T_{eff}$-correction and computed the Bayesian Information Criterion (BIC). Schwarz (1978) first proposed BIC as a way to choose between alternate models in regression where the model with the lowest BIC is the preferred. We used the weighted least squares (WLS) method from the *statsmodel* module in python to fit polynomials of order 0–7 and the step function. We found the BIC to be minimum for a first-order polynomial fit (BIC = -40.56) of the following form:

$$M_{spec} - M_{seis} = (0.39 \pm 0.05) M_{spec} + (-0.38 \pm 0.07). \quad (5)$$

However, a second order polynomial fit had a BIC of -37.72 with the difference in BIC ($\Delta$BIC) being 2.84. This value of $\Delta$BIC implies that the first order polynomial fit is a good fit to our mass offset(Fabozzi et al. 2014; Raftery 1995). However, we cannot completely rule out a second order polynomial fit either. Future work is needed to expand beyond the limits of the current study and comprehensively model the offset to potentially rule one out. Fig. 6 shows how well the first order polynomial model fits the mass offsets.

Despite the larger ensemble size used in this work, our study still suffers from a deficit of low-luminosity stars with spectroscopic masses below 1 $M_\odot$ and above 1.8 $M_\odot$.[10] From Table 2 (Column 5), we note that our low-luminosity solar-like oscillators covers a spectroscopic mass range of 0.91–2.19 $M_\odot$. As a result, we are unable to define how the mass offset behaves at masses well below 1 and well above 2 $M_\odot$. With TESS observing more evolved stars in the late subgiant/early red giant branch regime, future work might be able to explore the mass-dependent mass offset at sub-solar masses and masses above 2 $M_\odot$.

### 5.1.1 *A note on planet occurrence-mass-metallicity correlation*

Planets and stars form from the same gas cloud; hence the planet occurrence is believed to be closely related to fundamental stellar parameters like metallicity and stellar mass (Johnson et al. 2010; Ghezzi et al. 2018). While Malla et al. (2020) performed an ensemble analysis, their sample was too small to check the effect of their observed mass-dependent mass offset on the planet occurrence-mass-metallicity correlation. However, we now have a much larger sample with 451 stars, of which 76 stars have planets (according to the planetary systems table maintained by NASA Exoplanet archive[11]), allowing us to check for any effect of the mass offset on the planet occurrence-mass metallicity-correlation.

Like G18, we define planet occurrence as the ratio of the number of stars with planets to the total number of stars. Following G18, Figs. 7a and b depict planet occurrence as a function of stellar mass and metallicity for the low-luminosity stars in our sample. We computed two histograms, one representing the spectroscopic masses (filled) and the other representing the $\nu_{max}$-only based seismic masses (hatched) derived using the corresponding spectroscopic parameters ($T_{eff}$ and [Fe/H]). We only have a statistically significant sample for two (out of five) spectroscopic sources, namely W16 (Fig. 7a) and G18 (Fig. 7b). From both figures, we note that the median confidence intervals for the filled and hatched histograms are consistent with each other. Hence, we conclude that the planet occurrence-mass-metallicity correlation for spectroscopic and seismic masses is consistent with one another despite the observed mass offset. However, these results must be interpreted with caution due to the limited mass range of the sample.

We then applied Eq. 5 to the spectroscopic masses of 245 stars by Ghezzi et al. (2018) and plotted the planet occurrence for these stars as a function of mass and metallicity in Fig. 8. From this figure, we note that the histogram based on the offset-corrected spectroscopic masses (hatched light blue) is shifted to the right compared to the one based on the original spectroscopic masses (filled blue). However, the heights of individual bars are consistent within their corresponding confidence intervals. Hence, we conclude that the planet occurrence rate is not significantly affected by the perceived mass offset between the spectroscopic and seismic mass scales.

Our analysis finds that the observed mass offset does not affect the inferred planet occurrence rate. A possible explanation for this might be that the observed offset between the spectroscopic and seismic masses is so small relative to the strength of the correlation that the size of the discrepancy is not enough to cause large-scale systematic effects on the shape of the correlation. It is also possible that, instead of some of the masses being off or a significant mass

[9] The plots for individual spectroscopic source can be seen in Fig. A1

[10] Although the Malla et al. (2020) ensemble has three stars with spectroscopic masses greater than 2 $M_\odot$, they have not been observed by TESS during its three-year primary mission.

[11] DOI:10.26133/NEA12

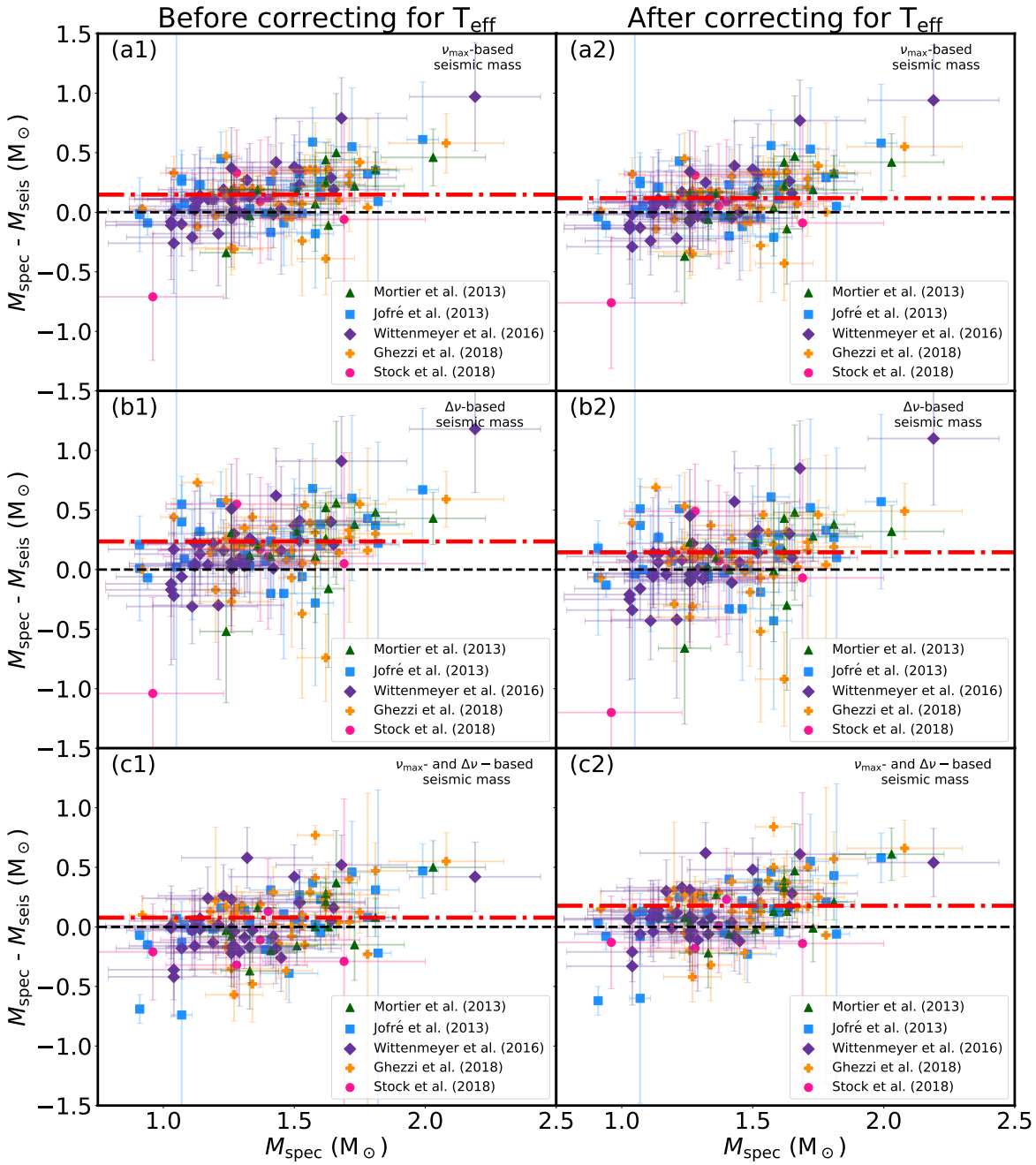


**Figure 5.** Difference between the spectroscopic and seismic mass plotted as a function of spectroscopic mass for 93 low-luminosity stars with solar-like oscillations. Column 1 depicts the mass offset before any corrections were made, and Column 2 depicts the mass offset after correcting the offset in the weighted average by decreasing the $T_{\rm eff}$ by 100K. The seismic masses used in panels a1 and a2 are the $\nu_{\rm max}$-only based seismic masses, in b1 and b2 are the $\Delta\nu$-only based seismic masses, and in c1 and c2 are the '$\nu_{\rm max}$ + $\Delta\nu$'- based seismic masses. The green triangles use the spectroscopic masses and parameter by M13 (14 stars), blue squares use those by J15 (31 stars), purple diamonds use those by W16 (36 stars), orange pluses use those by G18 (41 stars) and pink circles those by S18 (5 stars). The dashed black line represents no difference between the spectroscopic and seismic masses. The dash-dotted red line represents the weighted average mass offset.

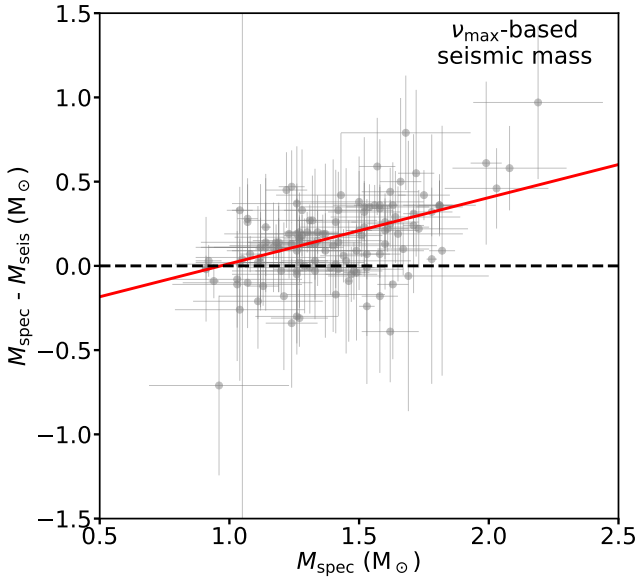


**Figure 6.** First order polynomial fit to the difference between the spectroscopic and seismic mass plotted as a function of spectroscopic mass for 93 low-luminosity stars with solar-like oscillations. We used the $\nu_{max}$-only based seismic masses ($M_1$) without any $T_{eff}$-correction applied. The solid red line represents an uncertainty-weighted least-squares fit to the data. The dashed black line represents no difference between the spectroscopic and seismic masses.

offset, the masses are systematically off. That is to say, massive stars are still massive, even though they are not as massive as the spectroscopic masses make them out to be. However, caution is advised when interpreting the results with the small sample size of the planet-hosting solar-like oscillators.

### 5.2 The high-luminosity stars

Of the 451 stars, we have 283 high-luminosity stars, according to the criteria listed in Sec. 2 (also marked individually in Table 3, column 11). The most luminous stars in this sample oscillate at frequencies too low to resolve with the length of our current TESS data. To be conservative, we do not report any seismic detections below a $\nu_{max}$ of 8 $\mu$Hz. Taking this hard detection limit into account, we have 160 solar-like oscillators, a spectroscopic source-wise breakdown of which is provided in Table 1 (columns 6–7). Similar to our low-luminosity sample, we compare our seismic masses to the spectroscopic masses by plotting the difference between the two as a function of spectroscopic mass in Fig. 9. We do not have a statistically significant high-luminosity star sample size for the spectroscopic sources M13, W16 and G18. Hence, these sources have been excluded from the figure and any discussion concerning the high luminosity stars.

From Fig. 9, we see a rather complicated mass offset. This observed offset is non-trivial to understand from a stellar evolution point, unlike the arguments used on the low-luminosity sample, where stellar tracks are well separated and non-overlapping. The high-luminosity stars are mostly in the region of the colour-magnitude diagram where the tracks clump together, making it harder to determine stellar mass using stellar models. Therefore, determining the stellar masses using a more model-independent method like asteroseismology might provide more robust stellar masses for these stars. However, the $\nu_{max}$-based seismic relation (Eq. 1) seems to break down for stars with radius larger than about 30-50 $R_\odot$ (Zinn et al. 2019b and Zinn et al. 2022, submitted), which affects up to 6 stars[12] in our sample.

## 6 CONCLUSIONS

We constructed a sample of 451 evolved stars from five different spectroscopic sources: M13, J15, W16, G18, and S18. Of the 451 stars, we found 253 solar-like oscillators from 2-min cadence TESS data and measured their $\nu_{max}$ and $\Delta\nu$.

To explore the mass-dependent mass offset between the spectroscopic and seismic masses for subgiants and red giants, we determined the seismic masses from three different scaling relations (Eqs. 1, 2 and 3) using spectroscopic parameters from M13, J15, W16, G18 and S18. We divided our initial sample into two subsets: 168 low- and 283 high-luminosity stars, such that the low-luminosity stars are synonymous with the previously studied retired A-stars (as defined by G18). Of these, we found 93 low- and 160 high-luminosity stars with solar-like oscillations. Comparing the spectroscopic and seismic masses for low-luminosity stars (mostly late subgiants and early red giants) reveals an increasing mass offset with mass between the two stellar mass scales. However, we found that the planet occurrence-mass-metallicity correlation does not significantly change when adopting the seismic masses. Despite our efforts to expand our ensemble size and to include more stars in the mass ranges not previously covered by Malla et al. (2020), our study is deficient in low-luminosity stars with spectroscopic masses well below 1 $M_\odot$ and above 2 $M_\odot$. A further study exploring these mass ranges may be needed to explore further the nature of the mass-dependent mass offset we observe.

We also found a mass offset between the spectroscopic and seismic masses for high-luminosity stars (primarily consisting of the red clump and more luminous stars). The observed offset may be attributed to the error-prone mass determination using isochrones due to the clumping together of evolutionary tracks in this region of interest. In addition to the comparison of spectroscopic and seismic mass scales, we provide a catalog (Table 4) of seismic masses and radii for the 253 solar-like oscillators in our primary sample derived using the $\nu_{max}$-based scaling relation (Eq. 1) and luminosities derived using TIC-based effective temperatures.

## ACKNOWLEDGEMENTS

We acknowledge support from the Australian Research Council through Discovery Project DP210103119. This paper includes data collected by the TESS mission, which are publicly available from the Mikulski Archive for Space Telescopes (MAST). Funding for the TESS mission is provided by NASA's Science Mission directorate. SPM thanks Joel C. Zinn for helping with parallax correction.

## DATA AVAILABILITY

The TESS data used in this article can be downloaded from TASOC (`www.tasoc.dk`). All the tables in this paper are available on CDS in a machine-readable format.

[12] namely, TIC 435443105, TIC 141326842, TIC 232074535, TIC 268804144, TIC 437310271, TIC 60905900

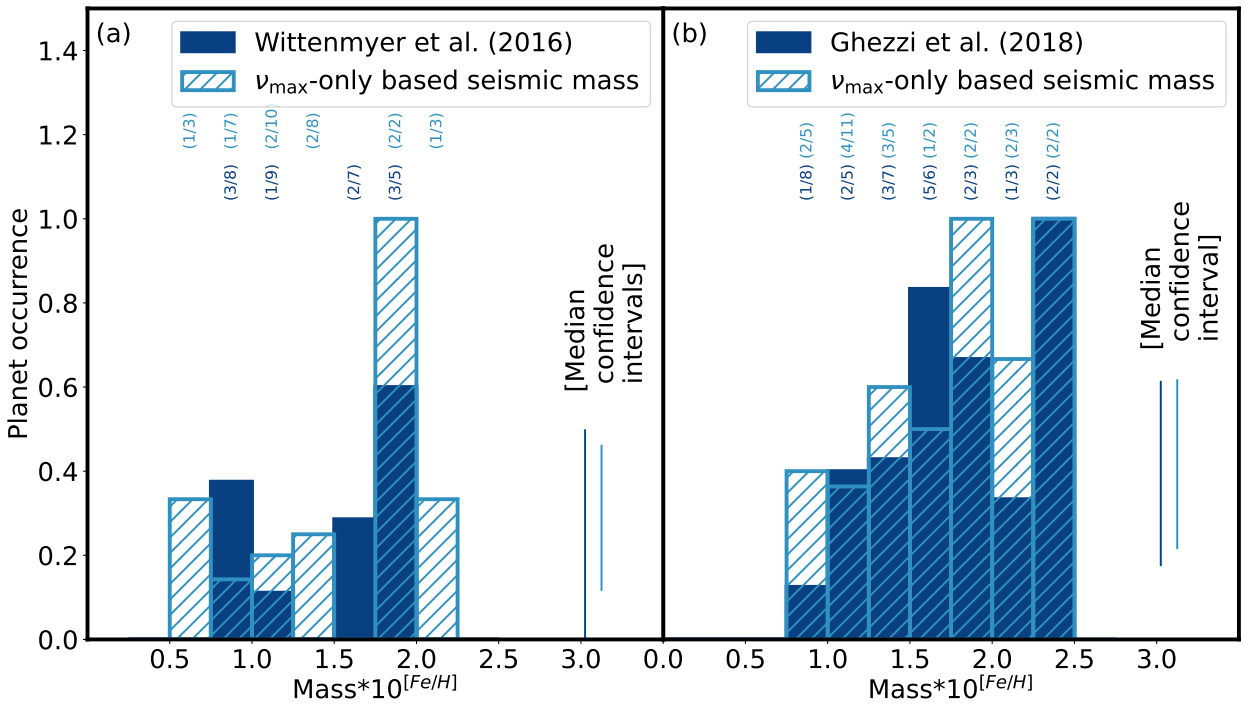


**Figure 7.** Planet occurrence plotted as a function of mass and metallicity. (a) The source used for the spectroscopic parameters is W16, corresponding to the filled dark blue histogram. The hatched light blue histogram uses the $\nu_{max}$-only based seismic masses derived using the spectroscopic parameters from W16. The bars in the histogram are annotated by the ratio of the number of stars with planets in each bin to the total number of stars in the bin. The ratio is colour-coded according to the corresponding histogram. The isolated solid lines indicate the median of the confidence intervals of the individual bars. They are colour-coded according to the spectroscopic or seismic mass plotted on the x-axis. (b) The spectroscopic source used here is G18.

## REFERENCES


Allende Prieto C., Lambert D. L., 1999, A&A, 352, 555

Andersen M. F., Grundahl F., Beck A. H., Pallé P., 2016, in Revista Mexicana de Astronomia y Astrofisica Conference Series. pp 54–58 (arXiv:1901.08293)

Berger T. A., Huber D., van Saders J. L., Gaidos E., Tayar J., Kraus A. L., 2020, AJ, 159, 280

Borucki W. J., et al., 2010, Science, 327, 977

Bovy J., Rix H.-W., Green G. M., Schlafly E. F., Finkbeiner D. P., 2016, ApJ, 818, 130

Brown T. M., Gilliland R. L., Noyes R. W., Ramsey L. W., 1991, ApJ, 368, 599

Campante T. L., et al., 2017, MNRAS, 469, 1360

Chaplin W. J., Miglio A., 2013, ARA&A, 51, 353

Corsaro E., Grundahl F., Leccia S., Bonanno A., Kjeldsen H., Paternò L., 2012, Astronomy & Astrophysics, 537, A9

Dawson R. I., Johnson J. A., 2018, ARA&A, 56, 175

Drimmel R., Cabrera-Lavers A., López-Corredoira M., 2003, A&A, 409, 205

Drimmel R., Bucciarelli B., Inno L., 2019, Research Notes of the American Astronomical Society, 3, 79

Fabozzi F., Focardi S., Rachev S., Arshanapalli B., Hoechstoetter M., 2014, The Basics of Financial Econometrics: Tools, Concepts, and Asset Management Applications. Frank J. Fabozzi Series, Wiley, https://books.google.co.in/books?id=3NrjAgAAQBAJ

Fischer D. A., Valenti J., 2005, ApJ, 622, 1102

Gaia Collaboration et al., 2016, A&A, 595, A1

Gaia Collaboration et al., 2018, A&A, 616, A1

Gaia Collaboration Vallenari, A. Brown, A.G.A. Prusti, T. et al. 2022a, A&A

Gaia Collaboration et al., 2022b, arXiv e-prints, p. arXiv:2208.00211

Gaulme P., et al., 2016, ApJ, 832, 121

Ghezzi L., Johnson J. A., 2015, ApJ, 812, 96

Ghezzi L., Montet B. T., Johnson J. A., 2018, ApJ, 860, 109

Girardi L., Groenewegen M. A. T., Hatziminaoglou E., da Costa L., 2005, A&A, 436, 895

Glebocki R., Gnacinski P., 2005, VizieR Online Data Catalog, p. III/244

Green G. M., et al., 2015, ApJ, 810, 25

Hey D. R., 2019, danhey/echelle: Initial release, doi:10.5281/zenodo.3403407, https://doi.org/10.5281/zenodo.3403407

Hjørringgaard J. G., Silva Aguirre V., White T. R., Huber D., Pope B. J. S., Casagrande L., Justesen A. B., Christensen-Dalsgaard J., 2017, MNRAS, 464, 3713

Høg E., 2000, Tycho Star Catalogs: The 2.5 Million Brightest Stars. p. 2862, doi:10.1888/0333750888/2862

Huber D., Stello D., Bedding T. R., Chaplin W. J., Arentoft T., Quirion P. O., Kjeldsen H., 2009, Communications in Asteroseismology, 160, 74

Huber D., et al., 2017, ApJ, 844, 102

Jenkins J. M., et al., 2016, in Proc. SPIE. p. 99133E, doi:10.1117/12.2233418

Jofré E., Petrucci R., Saffe C., Saker L., Artur de la Villarmois E., Chavero C., Gómez M., Mauas P. J. D., 2015, A&A, 574, A50

Johnson J. A., Marcy G. W., Fischer D. A., Henry G. W., Wright J. T., Isaacson H., McCarthy C., 2006, ApJ, 652, 1724

Johnson J. A., Aller K. M., Howard A. W., Crepp J. R., 2010, PASP, 122, 905

Johnson J. A., Morton T. D., Wright J. T., 2013, ApJ, 763, 53

Johnson J. A., et al., 2014, ApJ, 794, 15

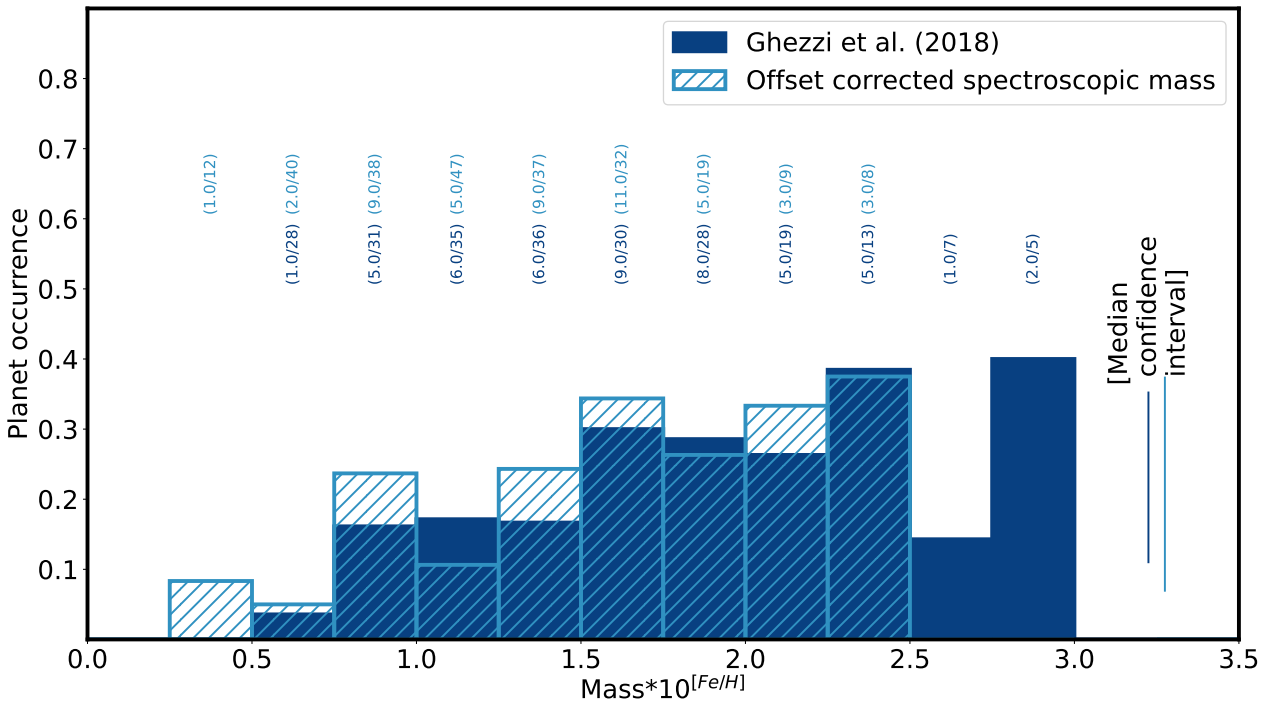


**Figure 8.** Planet occurrence plotted as a function of mass and metallicity for the sample by Ghezzi et al. (2018, G18, 245 stars). The dark blue histogram uses the spectroscopic masses and parameters by G18, while the hatched light blue histogram uses the offset-corrected spectroscopic masses using Eq. 5. The bars in the histogram are annotated by the ratio of the number of stars with planets in each bin to the total number of stars in the bin. The ratio is colour-coded according to the corresponding histogram. The isolated solid lines indicate the median of the confidence intervals of the individual bars. They are colour-coded according to the spectroscopic or seismic mass plotted on the x-axis.

Kallinger T., et al., 2010, A&A, 509, A77
Kjeldsen H., Bedding T. R., 1995, A&A, 293, 87
Lindegren L., et al., 2018, A&A, 616, A2
Lindegren L., et al., 2021, A&A, 649, A4
Lloyd J. P., 2011, ApJ, 739, L49
Lloyd J. P., 2013, ApJ, 774, L2
Malla S. P., et al., 2020, MNRAS, 496, 5423
Marshall D. J., Robin A. C., Reylé C., Schultheis M., Picaud S., 2006, A&A, 453, 635
Miglio A., et al., 2016, MNRAS, 461, 760
Mortier A., Santos N. C., Sousa S. G., Adibekyan V. Z., Delgado Mena E., Tsantaki M., Israelian G., Mayor M., 2013, A&A, 557, A70
North T. S. H., et al., 2017, MNRAS, 472, 1866
Pietrinferni A., Cassisi S., Salaris M., Castelli F., 2004, ApJ, 612, 168
Pinsonneault M. H., et al., 2014, ApJS, 215, 19
Pinsonneault M. H., et al., 2018, ApJS, 239, 32
Raftery A. E., 1995, Sociological Methodology, 25, 111
Ricker G. R., et al., 2016, in Space Telescopes and Instrumentation 2016: Optical, Infrared, and Millimeter Wave. p. 99042B, doi:10.1117/12.2232071
Schlaufman K. C., Winn J. N., 2013, ApJ, 772, 143
Schwarz G., 1978, The Annals of Statistics, 6, 461
Serenelli A., et al., 2017, ApJS, 233, 23
Sharma S., Stello D., Bland-Hawthorn J., Huber D., Bedding T. R., 2016, ApJ, 822, 15
Stassun K. G., et al., 2018, AJ, 156, 102
Stello D., Bruntt H., Preston H., Buzasi D., 2008, ApJ, 674, L53
Stello D., et al., 2011, ApJ, 739, 13
Stello D., et al., 2017, MNRAS, 472, 4110
Stock S., Reffert S., Quirrenbach A., 2018, A&A, 616, A33
Thygesen A. O., et al., 2012, A&A, 543, A160
Ulrich R. K., 1986, ApJ, 306, L37
White T. R., et al., 2018, MNRAS, 477, 4403
Wittenmyer R. A., Liu F., Wang L., Casagrande L., Johnson J. A., Tinney C. G., 2016, AJ, 152, 19
Wright J. T., 2005, PASP, 117, 657
Wright J. T., et al., 2011, PASP, 123, 412
Yu J., Huber D., Bedding T. R., Stello D., Hon M., Murphy S. J., Khanna S., 2018, ApJS, 236, 42
Zinn J. C., Pinsonneault M. H., Huber D., Stello D., 2019a, ApJ, 878, 136
Zinn J. C., Pinsonneault M. H., Huber D., Stello D., Stassun K., Serenelli A., 2019b, ApJ, 885, 166
van Leeuwen F., 2007, A&A, 474, 653

## APPENDIX A: MORE NOTES ON LOW-LUMINOSITY STARS

In Fig. 5, we plotted the difference between spectroscopic and seismic masses as a function of spectroscopic mass for all the spectroscopic sources together. However, to depict the mass offset for each spectroscopic source more clearly, we plot the mass offset separately for each source in Fig. A1. In Fig. A1, we depict the mass discrepancy between spectroscopic and seismic masses (plotted on the y-axis) as a function of the spectroscopic mass (plotted on the x-axis). Each row corresponds to a different spectroscopic source (rows a, b, c, d and e correspond to the spectroscopic masses by

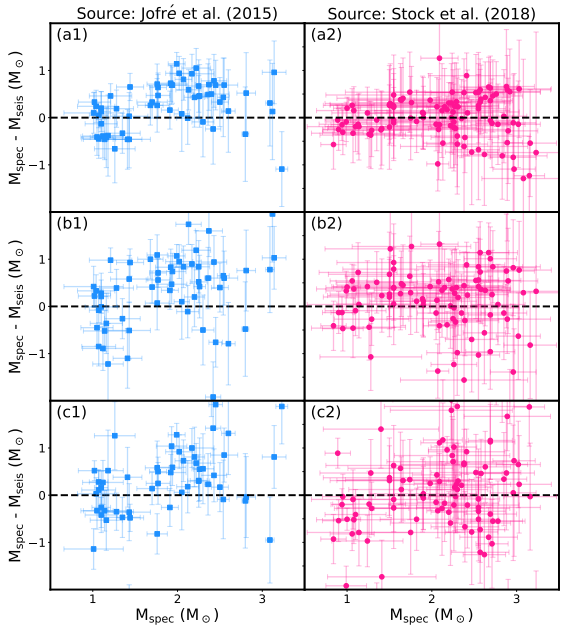


**Figure 9.** Difference between the spectroscopic and seismic mass plotted as a function of spectroscopic mass for 160 unique high-luminosity stars with solar-like oscillations, plotted separately according to the spectroscopic parameters used. The seismic masses used in row (1) are the $\nu_{\rm max}$-only based seismic masses, in row (2) are the $\Delta\nu$-only based seismic masses, and in row (3) are the'$\nu_{\rm max} + \Delta\nu$'- based seismic masses. The blue squares use the spectroscopic masses and parameters by Jofré et al. (2015, 62 stars) (Column 1), and pink circles use those by Stock et al. (2018, 114 stars) (Column 2). The black dashed line indicates zero difference between the spectroscopic and seismic masses.

M13, J15, W16, G18 and S18, respectively). At the same time, each column uses a different seismic mass (Columns 1, 2, and 3 correspond to the use of $\nu_{\rm max}$-only, $\Delta\nu$-only and '$\nu_{\rm max} + \Delta\nu$'-based seismic masses, respectively). 22 low-luminosity solar-like oscillators studied by multiple sources are plotted multiple times across different rows. From Fig. A1, we can see an increasing mass offset between spectroscopic and seismic masses across all the five different spectroscopic sources.

Also, in Figs. A1a1, b1 and e1, we plot alongside our results the difference between the spectroscopic and seismic masses for the ensemble previously studied by Malla et al. (2020) to compare the offsets in the two studies. We find our mass offset to be consistent with that found by Malla et al. (2020).

## APPENDIX B: A NOTE ON USE OF PARALLAXES

For computing luminosities using *isoclassify* in Sec. 4, we used parallaxes from three different sources: Gaia eDR3, DR2 and *Hipparcos*.

The Gaia eDR3 catalogue,[13] improves the precision by a factor of 1.5, compared to Gaia DR2 (Lindegren et al. 2021). So we prefer

[13] In this paper, we use Gaia eDR3 and DR3 synonymously because the Gaia DR3 builds upon the Gaia eDR3 catalogue (Gaia Collaboration et al. 2022b)

**Table B1.** Parallax sources used for our targets

| Source of Parallax | Criteria | Correction applied | $N_{\rm tot}$ | $N_{\rm tot,osc}$ |
|---|---|---|---|---|
| (1) | (2) | (3) | (4) | (5) |
| Gaia eDR3 | 6 < G < 21 | Lindegren et al. (2021) | 109 | 57 |
| Gaia DR2 | 5 ≤ G ≤ 6 | Zinn et al. (2019a) | 157 | 100 |
| *Hipparcos* | G<5 and exceptions | N/A | 186 | 96 |

Note: Exceptions include stars who do not have Gaia parallaxes, and stars whose fractional error in Gaia parallaxes is larger than in Hipparcos.
$N_{\rm tot}$: Number of stars in our entire sample for which we adopt the parallaxes available from source
$N_{\rm tot,osc}$: Number of oscillating stars in our sample for which we adopt the parallaxes available from source
G : Magnitude (`phot_g_mean_mag`) from Gaia eDR3. If not available, we used the magnitudes from Gaia DR2.
A machine-readable version of the table is available as online downloadable material and from CDS.

Gaia eDR3 parallaxes for our targets if they are available. However, despite the precision improvement, the Gaia eDR3 parallaxes suffer from systematic offsets and must be corrected for a zero-point offset. For our Gaia eDR3 parallaxes, we use the python code[14] by Lindegren et al. (2021) to compute the zero-point offset based on the position, colour and magnitude of the star. The zero-point offsets are then subtracted from the Gaia eDR3 parallaxes. However, these corrections can only be applied to stars with $6 < G < 21$. To overcome these limitations, we only use the Gaia eDR3 parallaxes for stars with $6 < G < 21$ and Gaia DR2 parallaxes for stars with $G < 6$. We corrected our Gaia DR2 parallaxes using an `astrometric_pseudocolor`- and magnitude-based relation given by Zinn et al. (2019a).

We know that Gaia DR2 parallaxes are prone to calibration issues for stars brighter than G = 5 (Drimmel et al. 2019). Hence, we used Hipparcos parallaxes for stars with G < 5. Also, we do not have any Gaia eDR3/DR2 measurement available for 66 stars. For these 66 stars, we use *Hipparcos* parallaxes instead. We also use *Hipparcos* parallaxes for three stars that have a larger fractional error in Gaia parallaxes than in *Hipparcos*.

By comparing the corrected eDR3 parallaxes to the DR2 ones for the stars that have both measurements, we obtain a median fractional difference of about 0.6% between the two parallaxes measurements. For five solar-like oscillators,[15] we find the fractional difference to be more than 5%, but less than 32%. A possible reason for a larger fractional difference for these stars is due to the improvement in parallaxes from Gaia DR2 to eDR3. In conclusion, we find that the parallaxes from Gaia eDR3 corrected using the code by Lindegren et al. (2021) and from Gaia DR2 corrected using the relation by Zinn et al. (2019a) are consistent with each other.

Table B1 summarises our discussion on the use of parallaxes in this paper. We also provide the source of parallax for each solar-like oscillator in Table 4 (Column 8).

This paper has been typeset from a TEX/LATEX file prepared by the author.

[14] https://gitlab.com/icc-ub/public/gaiadr3_zeropoint
[15] TIC 29921672, TIC 422279419, TIC 156291668, TIC 165193011, and TIC 5630694

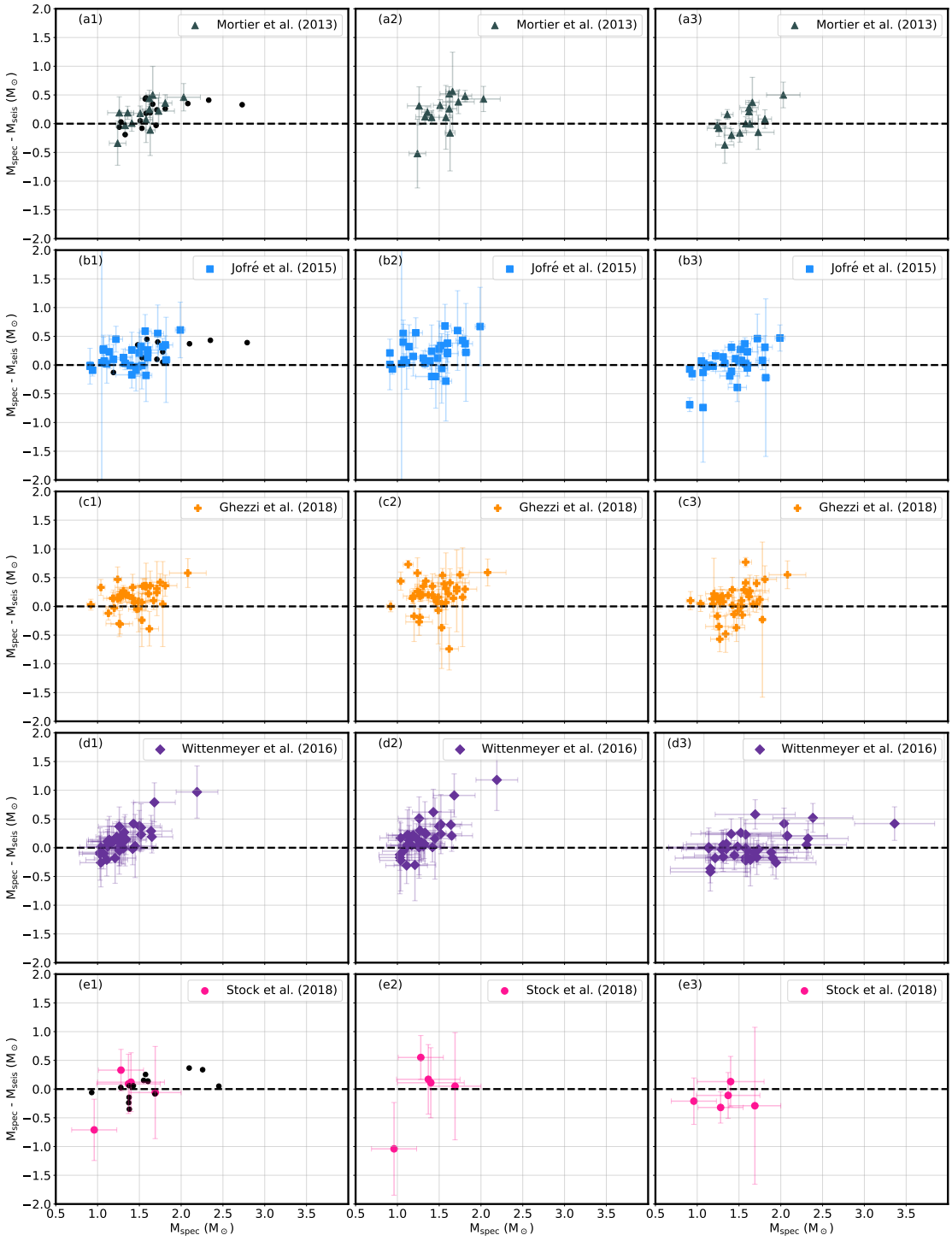


**Figure A1.** Difference between the spectroscopic and seismic mass plotted as a function of spectroscopic mass for 93 unique low-luminosity stars with solar-like oscillations, plotted separately according to the spectroscopic parameters used. The seismic masses used in column (1) are the $\nu_{\rm max}$-only based seismic masses, in column (2) are the $\Delta\nu$-only based seismic masses, and in column (3) are the'$\nu_{\rm max}$ + $\Delta\nu$'- based seismic masses. The green triangles use the spectroscopic masses and parameters by M13 (14 stars, row a), blue squares use those by J15 (31 stars, row b), purple diamonds use those by W16 (36 stars, row c), orange pluses use those by G18 (41 stars, row c) and pink circles those by S18 (5 stars, row e). The black dashed line indicates zero difference between the spectroscopic and seismic masses.The black square points in (a1), (b1) and (e1) correspond to the results from ensemble study by Malla et al. (2020).